RESEARCH ARTICLE-PHYSICS

Numerical Treatments to Analyze the Nonlinear Radiative Heat Transfer in MHD Nanofluid Flow with Solar Energy

Saeed Ehsan Awan[1] · Muhammad Asif Zahoor Raja[1,2] · Ammara Mehmood[3] · Shahab Ahmad Niazi[4] · Sadia Siddiqa[5]

Abstract
In the current study, the nonlinear radiative heat transfer effects due to solar radiation in magneto-hydrodynamic (MHD) nanofluidic problem are analyzed effectively by novel application of numerical computing by Adams predictor–corrector and explicit backward difference solvers. The governing relations of PDEs for the model are transformed into the system of ODEs, and numerical solvers are applied to the transformed system to study the effect of radiation parameter along with thermophoresis parameter, Brownian motion parameter, magnetic field parameter, Lewis number, Prandtl number, Eckert number and Biot number on velocity, temperature and nanoparticle concentration profiles. The comparative study of both solvers is provided in sufficient number of graphical and numerical illustrations to prove the worth in terms of accuracy, robustness and stability.

Keywords Nanofluid · Numerical computing · Solar radiation · Heat transfer · MHD

✉ Ammara Mehmood
  ammara.mehmood@adelaide.edu.au

  Saeed Ehsan Awan
  saeed.ehsan@ciit-attock.edu.pk

  Muhammad Asif Zahoor Raja
  muhammad.asif@ciit-attock.edu.pk

  Shahab Ahmad Niazi
  shahabniazi@iub.edu.pk

  Sadia Siddiqa
  saadiasiddiqa@gmail.com

[1] Department of Electrical and Computer Engineering, COMSATS University Islamabad, Attock Campus, Attock 43600, Pakistan

[2] Future Technology Research Center, National Yunlin University of Science and Technology, 123 University Road, Section 3, Douliou, Yunlin 64002, Taiwan, R. O. C.

[3] School of Electrical and Electronic Engineering, The University of Adelaide, Adelaide, SA, Australia

[4] Department of Electronic Engineering, Engineering College, The Islamia University of Bahawalpur, Bahawalpur 63100, Pakistan

[5] Department of Mathematics, COMSATS University Islamabad, Attock Campus, Attock 43600, Pakistan

List of Symbols

(u, w)	Components of velocity profile
(U, W)	Coordinate axes
T	Fluid temperature
p	Fluid pressure
υ	Dynamic viscosity
C	Nanoparticle concentration
q_r	Radiative heat flux parameter
H_0	Strength of uniform magnetic field
D_B	Brownian parameter
D_T	Thermophoretic diffusion parameter
R_d	Radiation parameter
N_t	Thermophoresis parameter
N_b	Brownian motion parameter
M	Magnetic parameter
Le	Lewis Number
Pr	Prandtl number
E_c	Eckert number

Greek Symbols

ρ	Density
σ^*	Stefan–Boltzmann constant

Springer

k^*	Mean absorption coefficient
ρ_f	Based fluid density
α	Based fluid thermal diffusivity
$f(\eta)$	Velocity Profile
$\theta(\eta)$	Temperature Profile
$\phi(\eta)$	Concentration Profile
$u_w(x)$	Stretching velocity along horizontal axis
$u_\infty(x)$	Free stream velocity
$(\rho c)_f$	Heat capacity of fluid
$(\rho c)_p$	Heat capacity of nanofluid
γ	Biot number
σ_e	Electrical Conductivity
λ	Ratio of rates of free stream velocity to stretching sheet velocity
τ	Ratio of heat capacity of nanoparticle to heat capacity of fluid

1 Introduction

Sun is the most prognosticating renewable energy source and also the ultimate alternative to fossil fuels. The sun light can be converted to electricity by photoelectric effect and to heat through photothermal conversion. Both the photoelectric effect and photothermal conversion processes are being applied to generate electricity using photovoltaic panels and concentrated solar thermal plants. The efficiency of photovoltaic cells and concentrated solar thermal plants can be improved appreciably by increasing the solar absorption. The solar energy efficient absorption and conversion into thermal energy are required to reliably use as renewable source and to reduce the dependence on fossil fuels. However, the absorption of sunlight by collecting panels and heat collector tubes is quite inefficient that causes significant loss of energy. Therefore, water dispersed nanoparticles are being investigated quite extensively to improve the absorption of sunlight. Different research groups have proposed and tested different nanomaterials for increase in absorption efficiency.

Photoactive nanomaterials are proposed to enhance the light absorption capability of polymeric photovoltaic devices. The current polymer photovoltaic devices have active region (bandgap) of around 2-ev to absorb photons. The wider solar energy band absorption above specified bangap can be achieved by adding nanomaterials. Kim et al. fabricated solar cells by employing organic substances as two hemicyanine photosensitizer, and electronic intercessor for n-type titanium dioxide (TiO2) nanotube arrays of varying π-coupling lengths that have wider solar absorption spectrum from visible to near-infrared region [1]. Wild et al. utilized increased light sensitivity of silane (Si–H4) to form a solar up-converter for sub-bandgap light by exciting it with wide spectrum light [2]. Hua et al. examined the possibility of large-size heterojunction solar cells by converting hori-

zontally oriented single-crystalline silicon (c–Si) core/shell into half-coaxial nanowires arrays [3]. Pakhuruddin et al. proposed liquid-phase crystallization of Si films on textured glass with large light quality grain of 27.8 mA/cm^2 in solar cells or 36.3% enhancement compared with a planar reference film without light-trapping features [4]. Ishizaki et al. investigated the direct surface etched microcrystalline silicon (μc–Si) photovoltaic cells, where intrinsic microcrystalline layer intensified through raising the coupling of resonant modes of incident light. They reported 11% increase in efficiency for microcrystalline photovoltaic cell composed of intrinsic Si [5]. Chen et al. proposed that a two-dimensional perovskite solar cell (PSC) with absorption efficiency reaches 65.7% over the visible range for a 100-nm-thick perovskite layer [6]. Mehmood et al. reported 7.9% absorption improvement by applying lead xanthate spray on titanium dioxide outer boundary to implant lead sulfide (PbS) nanocrystals in dye-sensitized solar cells [7]. Liang et al. proposed that a light intensity detector with density sensitivity reaches 1.5291 dB/(mW-mm) embellished by microstructured optical fiber (MOF) with two air holes in the innermost layer instilled with ionic liquid between two segments [8]. Satoshi Ishii et al. numerically proved the increase in solar energy absorption by immersing the transition metal nitrides and carbides in water, which they later also verified through experimental results [9]. Raffaelle et al. demonstrated the synthesis of indium antimonide (InSb) quantum dots for better absorption efficiency in long infrared region of the solar spectrum. They discovered that nanoparticles doped with rare earth oxides can raise photons to energies above the bandgap energy of polymers [10]. Gondal et al. showed that absorption can be enhanced for visible range by spraying anatase phase semispherical titanium dioxide (TiO$_2$) nanoparticles along with 3–4-nm gold particles on TiO$_2$ surface compared to absorption of copper-doped TiO$_2$ or pure TiO$_2$ [11]. Hogan et al. adjudged that the steam could be produced in aqueous solutions containing light-absorbing nanoparticles when exposed to sun light at the bulk fluid temperature much lower than its boiling point [12]. Ishii et al. demonstrated experimentally that sprinkling of silicon nanoparticles in water has acted as splendid solar heat transducers to utilize solar energy for quick vaporization of water [13]. Hameed et al. reported an increase in efficiency of one-meter optical energy receiver with glass-to-copper tube size ratio of (1/4), (1/2) and (3/4) of flow rate up to 51.8%, 61% and 47%, respectively, through numerical model for inclined receiver tube with flowing water under thermosiphon effect and nanofluid annular region [14]. Wang et al. demonstrated that heat deposit ability and light-to-heat conversion of the plasmonic nanocomposites could be improved by altering nanocomposites ratios [15]. Mushtaq et al. studied Rosseland approximation for thermal radiation and simplified the governing equations by transforming boundary

layer into dimensionless form through Runge–Kutta method (RKM) transformations by exploiting appropriate shooting technique [16]. Ghasemi et al. conducted a numerical study to understand the effect of light radiation on the magneto-hydrodynamic (MHD) nanofluid flow by applying Rosseland approximation through Keller–Box numerical method [17]. Besides these, there are many reported studies in which the dynamics of nanofluidic problems are investigated in diversified fields; see [18–34] and references cited therein.

In the current study, the analysis of the nanofludics system is carried out numerically with following highlights in terms of salient features as:

- Novel application of numerical solvers is presented to study the effects of the nonlinear radiative heat transfer due to solar radiation in MHD fluid flow mixed with nanomaterial using the competency of Adams and explicit backward finite difference approaches.
- Similarity transformation is exploited for reduction of partial differential equations (PDEs) to system of ordinary differential equations (ODEs).
- The dynamics of the system by mean of velocity, temperature and nanoparticle concentration profiles are presented to study the effects of radiation parameter for, thermophoresis, Brownian motion, magnetic field, Lewis, Prandtl, Eckert and Biot numbers.
- The comparative study through graphical and numerical illustrations established the worth of the solvers in terms of accuracy, robustness and stability for analysis of the model.

Rest of the paper organized as follows: The system model of nanofluidic problem is given in Sect. 2, the overview of the proposed numerical solvers is presented in Sect. 3, results of numerical experimentation are provided in Sect. 4, conclusions are listed in Sect. 5 while convergence and complexity analysis is provided in Sect. 6.

2 System model

Let us assume the nanomaterial mixed flow over a stretched wall with convectively heated at $y=0$. The stretching velocity along horizontal axis is $u_w = ax$, whereas the free stream velocity is $u_\infty(x) = bx$. Magnetic field having strength H_0 is introduced perpendicularly to the flow. The analysis of heat transfer is considered in the presence of Joule heating, thermal radiation and impact of viscous dissipation. The combined influence of Brownian motion and thermophore-

sis is also considered. The governing relations for the flow model are given as follows: [16, 17]

$$\frac{\partial u}{\partial x} + \frac{\partial v}{\partial y} = 0 \tag{1}$$

$$u\frac{\partial u}{\partial x} + v\frac{\partial u}{\partial y} = u_\infty \frac{du_\infty}{\partial x} + v_f \frac{\partial^2 u}{\partial y^2} - \frac{\sigma_e H_0^2}{\rho_f}(u - u_\infty) \tag{2}$$

$$u\frac{\partial T}{\partial x} + v\frac{\partial T}{\partial y} = \alpha \frac{\partial^2 T}{\partial y^2} + \frac{v_f}{C_f}\left(\frac{\partial u}{\partial y}\right)^2$$
$$- \frac{1}{(\rho C)_f}\frac{\partial q_r}{\partial z} + \frac{\sigma_e H_0^2}{(\rho C)_f}(u_\infty - u)$$
$$+ \tau D_B\left(\left(\frac{\partial T}{\partial y}\frac{\partial C}{\partial y}\right) + \frac{D_T}{T_\infty}\left(\frac{\partial T}{\partial y}\right)^2\right), \tag{3}$$

$$u\frac{\partial C}{\partial x} + v\frac{\partial C}{\partial y} = D_B\left(\frac{\partial^2 C}{\partial y^2}\right) + \frac{D_T}{T_\infty}\left(\frac{\partial^2 T}{\partial y^2}\right). \tag{4}$$

In Eqs. (1–4), u and v are velocity components in the direction of x-axis and y-axis, respectively, $\upsilon = {\mu}/{\rho_f}$ stands for the dynamic viscosity, ρ_f denotes the density of the base fluid, $\alpha = {k}/{(\rho C)_f}$ is the based fluid thermal diffusivity, $(\rho C)_f$ and $(\rho C)_p$ represent the heat capacities, C is nanoparticle concentration, q_r is the radiative heat flux parameter, D_B and D_t are coefficients for the Brownian and thermophoretic diffusion parameter, respectively. The radiative heat flux relations are given mathematically as follows:

$$q_r = -\frac{4\sigma^*}{3k^*}\frac{\partial T^4}{\partial y} = -\frac{4\sigma^*}{3k^*}T^3\frac{\partial T}{\partial y} \tag{5}$$

where σ^* is the Stefan–Boltzmann constant while k^* is the mean absorption coefficient. The set of differential equations (Eqs. 2–4) are transformed into ODEs given by

$$\frac{d^3 f}{d\eta^3} + f\frac{d^2 f}{d\eta^2} - \left(\frac{df}{d\eta}\right)^2 + M\left(\lambda - \frac{df}{d\eta}\right) = 0, \tag{6}$$

$$\left[1 + R_d\left(1 + (\theta_w - 1)\theta^3\right)\frac{d\theta}{d\eta}\right]' + \Pr f\frac{d\theta}{d\eta}$$
$$+ \Pr N_b\frac{d\theta}{d\eta}\frac{d\phi}{d\eta} + \Pr N_t\left(\frac{d\theta}{d\eta}\right)^2 + \Pr E_c\left(\frac{d^2 f}{d\eta^2}\right)^2$$
$$+ \Pr M E_c\left(\lambda - \frac{df}{d\eta}\right)^2 = 0, \tag{7}$$

$$\frac{d^2\varphi}{d\eta^2} + Le f\frac{d\varphi}{d\eta} + \frac{N_t}{N_b}\frac{d^2\theta}{d\eta^2} = 0 \tag{8}$$

Along with wall properties

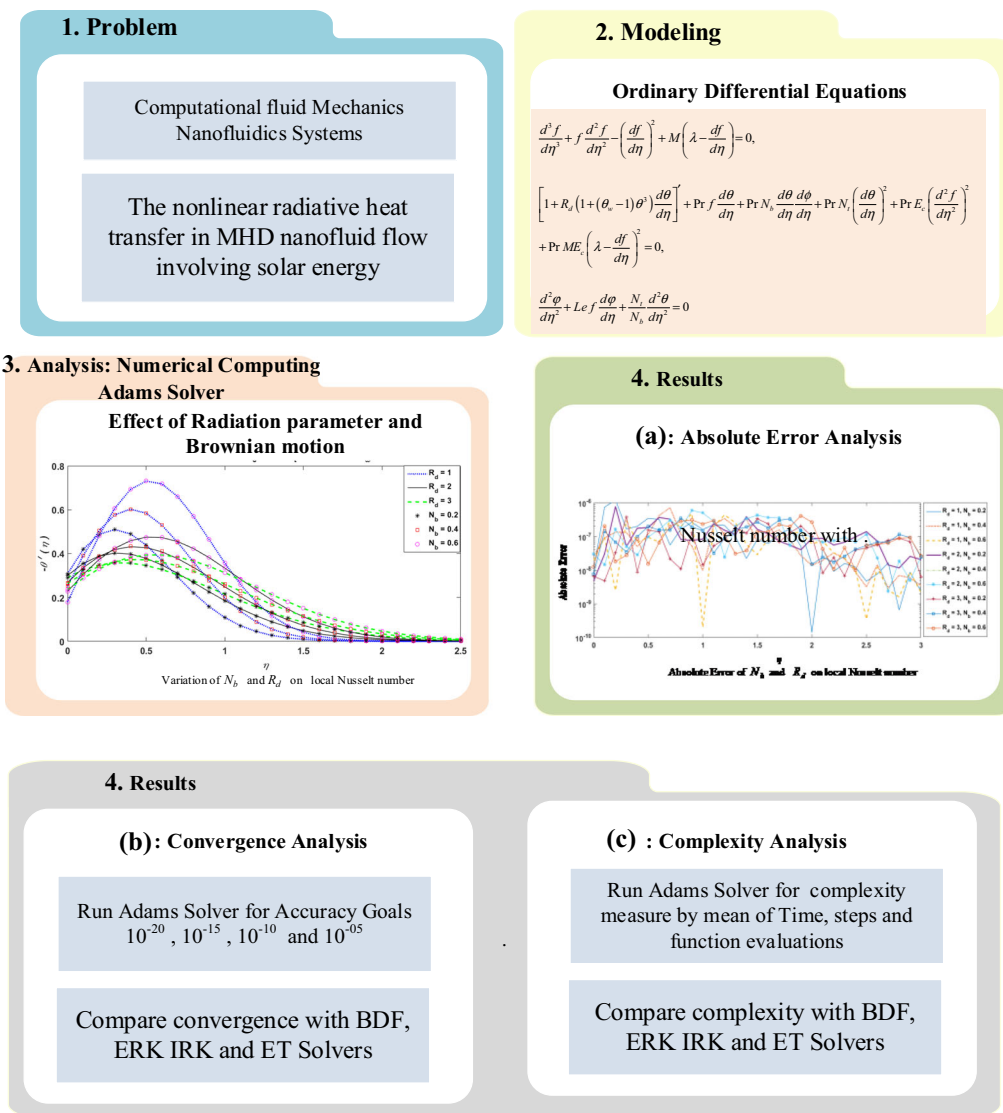$$f(0) = 0, f'(0) = 1, f'(\infty) \to \lambda$$

Fig. 1 Workflow graph of proposed study for analysis of heat transfer in MHD nanofluid flow

$$\theta'(0) = -\gamma[1 - \theta(0)], \Phi(0) = 1, \theta(\infty) \to 0, \Phi(\infty) \to 0 \tag{9}$$

The surface heat and mass fluxes in dimensionless form are given by

$$\frac{Nu_x}{\sqrt{\text{Re}_x}} = -\Big[1 + R_d\theta_w^3\Big]\theta'(0) = Nur,$$

$$\frac{Sh}{\sqrt{\text{Re}_x}} = -\phi'(0) = Shr. \tag{10}$$

3 Numerical Procedure

In the current study, we have exploited the strength of Adams predictor–corrector method along with backward difference

method (BDF) [18–22] to solve the system of Eqs. (6–8) by using boundary conditions as given in Eq. (9). The generic workflow graph of the proposed study is presented in Fig. 1.

3.1 Numerical Solver: Adams Method

To solve the ODEs, the Adam numerical method is used. In this method, predictor solution is predicted firstly; then, corrector is used to find the accurate solution by using already calculated solution. Considering Eqs. (7–8) in case of velocity, temperature and concentration profile as:

$$\frac{df}{d\eta} = v(\eta, f), \quad f(\eta_0) = f_0, \tag{11}$$

$$\frac{d\theta}{d\eta} = v(\eta, \theta), \quad \theta(\eta_0) = \theta_0, \tag{12}$$

Table 1 Local Nusslet and local Sherwood numbers for parameters $\gamma = 0.5$, $Pr = 7$ and $E_c = 0.1$, $L_e = 1$

R_d	N_t	N_b	M	$-\theta'(0)$	$-\varphi'(0)$	$\theta(0)$
1	0.1	0.1	0.5	0.3014483705176	1.2311834022170	0.39710325896467
1	0.3	0.1	0.5	0.2619694383282	1.7624692440389	0.47606112334350
1	0.5	0.1	0.5	0.17142054855713	3.52967121793032	0.65715890288573
2	0.1	0.1	0.5	0.31533213675252	1.19192659050101	0.3693357264949
2	0.3	0.1	0.5	0.29927518635443	1.43766242090081	0.4014496272911
2	0.5	0.1	0.5	0.27776424408246	1.95731196029044	0.4444715118350
3	0.1	0.1	0.5	0.32066102420717	1.17688369302784	0.35867795158565
3	0.3	0.1	0.5	0.310655611908026	1.33861996113379	0.3786887761839
3	0.5	0.1	0.5	0.29868978767185	1.64973278534274	0.4026204246562
1	0.1	0.2	0.5	0.2564201872151	1.2526118407327	0.4871596255696
1	0.1	0.4	0.5	0.13618200243445	1.28647096406646	0.7276359951310
1	0.1	0.6	0.5	0.01187246108135	1.30114271317503	0.9762550778372
2	0.1	0.2	0.5	0.29366415478741	1.1986894491540	0.41267169042516
2	0.1	0.4	0.5	0.242674103431474	1.20794770025336	0.5146517931370
2	0.1	0.6	0.5	0.183444800068997	1.21537302943055	0.6331103998620
3	0.1	0.2	0.5	0.30640925545029	1.18018059038463	0.38718148909941
3	0.1	0.4	0.5	0.27453937422510	1.1844167713514	0.4509212515497
3	0.1	0.6	0.5	0.23855690229302	1.18796791701035	0.5228861954139
1	0.1	0.1	0	0.34325013189817	1.10920838429727	0.31349973620364
1	0.1	0.1	1	0.330017205409986	1.14579951607939	0.33996558918002
1	0.1	0.1	2	0.31764531528230	1.18021087245646	0.3647093694353
2	0.1	0.1	0	0.33950030467008	1.12155047006559	0.3209993906598
2	0.1	0.1	1	0.33186994559330	1.14177216353678	0.33626010881338
2	0.1	0.1	2	0.324856289690489	1.16048870381786	0.3502874206190
3	0.1	0.1	0	0.33769704470676	1.12752316471445	0.324605910586463
3	0.1	0.1	1	0.3323256558234246	1.1410992265350	0.33534868835315
3	0.1	0.1	2	0.3274166772877258	1.15361198452883	0.34516664542454

$$\frac{d\varphi}{d\eta} = v(\eta, \varphi), \quad \varphi(\eta_0) = \varphi_0, \tag{13}$$

Adams–Moulton two-step predictor relations in case of profiles for temperature and concentration are given as:

$$f_{k+1} = f_k + \frac{h}{2}(3v(\eta_k, f_k) - v(\eta_{k-1}, f_{k-1})), \tag{14}$$

$$\theta_{k+1} = \theta_k + \frac{h}{2}(3v(\eta_k, \theta_k) - v(\eta_{k-1}, \theta_{k-1})), \tag{15}$$

$$\varphi_{k+1} = \varphi_k + \frac{h}{2}(3v(\eta_k, \varphi_k) - v(\eta_{k-1}, \varphi_{k-1})), \tag{16}$$

while the two-step corrector formulas for Adams–Moulton are given by

$$f_{k+1} = f_k + \frac{h}{2}(v(\eta_{k+1}, f_{k+1}) - v(\eta_k, f_k)), \tag{17}$$

$$\theta_{k+1} = \theta_k + \frac{h}{2}(v(\eta_{k+1}, \theta_{k+1}) - v(\eta_k, \theta_k)), \tag{18}$$

$$\varphi_{k+1} = \varphi_k + \frac{h}{2}(v(\eta_{k+1}, \varphi_{k+1}) - v(\eta_k, \varphi_k)), \tag{19}$$

Accordingly, the four-step Adam-Moulton predictor corrector expressions can be seen in literature [18].

4 Implicit Backward Difference Method

Backward difference method (BDF) uses method of numerical integration to solve system of ODEs Eqs. (6–8) by using boundary conditions as given in Eq. (9). The general expression for the method is given by

$$\sum_{k=0}^{s} d_k v_{n+k} = dw f(t_{n+s}, u_{n+s}), \tag{20}$$

In the above equation, d represents the step size. For the maximum convergence coefficient d and W are incorporated as follows

$$v_{n+1} - v_n = df(t_{n+1}, u_{n+1}), \tag{21}$$

Table 2 Local Nusslet and local Sherwood numbers for $N_t = N_b = 0.1$ and $M = 0.5$

R_d	Pr	E_c	L_e	γ	$-\theta'(0)$	$-\varphi'(0)$	$\theta(0)$
1	1	0.2	1	0.5	0.3274981328394	1.1575231251804	0.345003734321
1	4	0.2	1	0.5	0.3131890743903	1.1979726181008	0.373621851219
1	7	0.2	1	0.5	0.3014483705176	1.2311834022170	0.397103258964
2	1	0.2	1	0.5	0.3303279970274	1.1494791704376	0.33934400594
2	4	0.2	1	0.5	0.3222854214918	1.1722918326150	0.35542915701
2	7	0.2	1	0.5	0.3153321367525	1.1919265905010	0.36933572649
3	1	0.2	1	0.5	0.3313092205783	1.1466851021423	0.33738155884
3	4	0.2	1	0.5	0.3256989339769	1.1626271708526	0.34860213204
3	7	0.2	1	0.5	0.3206610242071	1.1768836930278	0.35867795158
1	7	0.1	1	0.5	0.33651586894126	1.1278009205925	0.32696826217
1	7	0.4	1	0.5	0.22915948072399	1.4443555068010	0.54168103851
1	7	0.7	1	0.5	0.11479968660242	1.7817672252021	0.77040062675
2	7	0.1	1	0.5	0.33560016921708	1.1318680124054	0.32879966152
2	7	0.4	1	0.5	0.27442374596699	1.3131649876766	0.45115250806
2	7	0.7	1	0.5	0.21210529208903	1.4979025729936	0.57578941582
3	7	0.1	1	0.5	0.33494744550269	1.1344577474642	0.33010510890
3	7	0.4	1	0.5	0.29196377518948	1.2621119867538	0.41607244962
3	7	0.7	1	0.5	0.24860307927663	1.3909071949841	0.50279384142
1	7	0.1	1	0.5	0.33651586894126	1.1278009205925	0.32696826217
1	7	0.1	3	0.5	0.33180348980369	1.4243867829370	0.33639302039
1	7	0.1	5	0.5	0.32760757559780	1.7181688425150	0.34478484888
2	7	0.1	1	0.5	0.33560016921708	1.1318680124054	0.32879966156
2	7	0.1	3	0.5	0.33328452460812	1.4234910064825	0.33343095075
2	7	0.1	5	0.5	0.33128636954072	1.7122788965761	0.33742726094
3	7	0.1	1	0.5	0.33494744550269	1.1344577474642	0.33010510890
3	7	0.1	3	0.5	0.33341013255039	1.4248226633462	0.33317973480
3	7	0.1	5	0.5	0.33209646378764	1.7123539096130	0.33580707242
1	7	0.1	1	0.1	0.08567996957979	1.1962403995524	0.14320030420
1	7	0.1	1	0.4	0.28493933187586	1.1403749779741	0.28765167031
1	7	0.1	1	0.7	0.42336685355857	1.1086015629350	0.39519020924
2	7	0.1	1	0.1	0.08769241318855	1.1751371370026	0.12307586811
2	7	0.1	1	0.4	0.28552570981476	1.1395591044728	0.28618572547
2	7	0.1	1	0.7	0.41916217619399	1.1203051797367	0.40119689987
3	7	0.1	1	0.1	0.08857457721123	1.1658260185034	0.114254227622
3	7	0.1	1	0.4	0.28558038525431	1.1399435618224	0.286049036866
3	7	0.1	1	0.7	0.41700645631089	1.1262736648986	0.404276444355

thus,

$$v_{n+6} - \frac{360}{147} v_{n+5} + \frac{450}{147} v_{n+4} - \frac{400}{147} v_{n+3}$$
$$+ \frac{225}{147} v_{n+2} - \frac{72}{147} v_{n+1} + \frac{10}{147} v_n$$
$$- \frac{60}{147} df(t_{n+6}, v_{n+6}) = 0. \tag{22}$$

5 Numerical Results with Interpretations

The analysis on the effect of solar radiation in the presence of magnetic field over stretched plate on a nanofluid boundary layer by using Adams and BDF methods is presented here. We have described the influence of radiation parameter R_d along with thermophoresis parameter N_t, Brownian motion parameter N_b, magnetic field parameter M, Lewis number Le, Prandtl number Pr, Eckert number E_c and Biot number γ on temperature profile $\theta(\eta)$, nanoparticle concentration profile $\phi(\eta)$, local Nusselt and local Sherwood

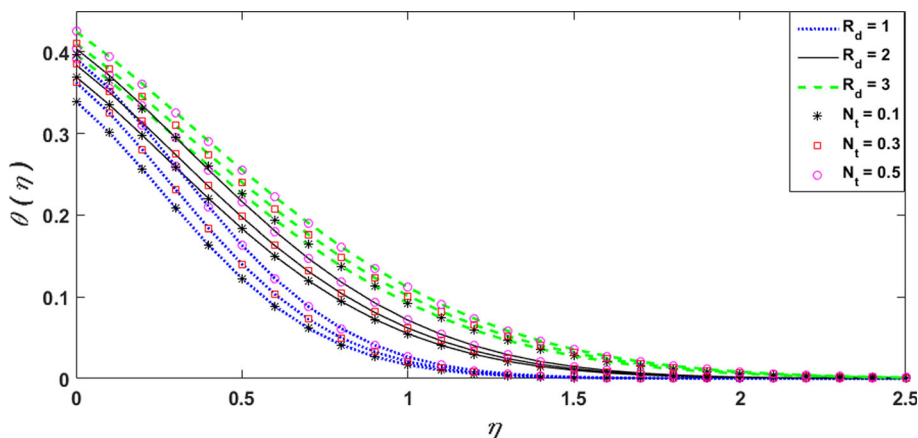**Fig. 2** Influence of N_t and R_d on $\theta(\eta)$

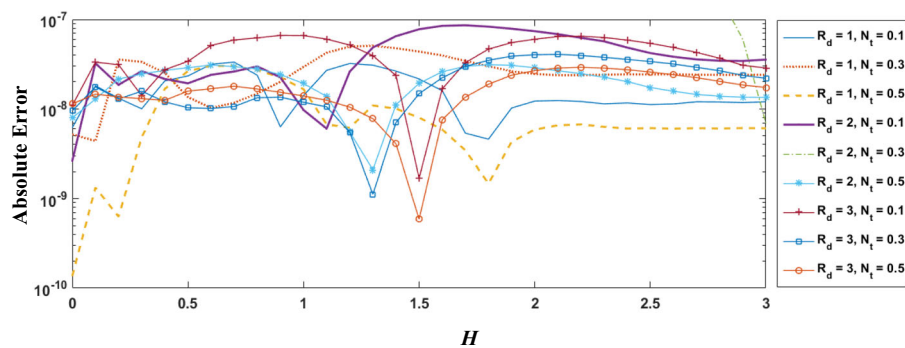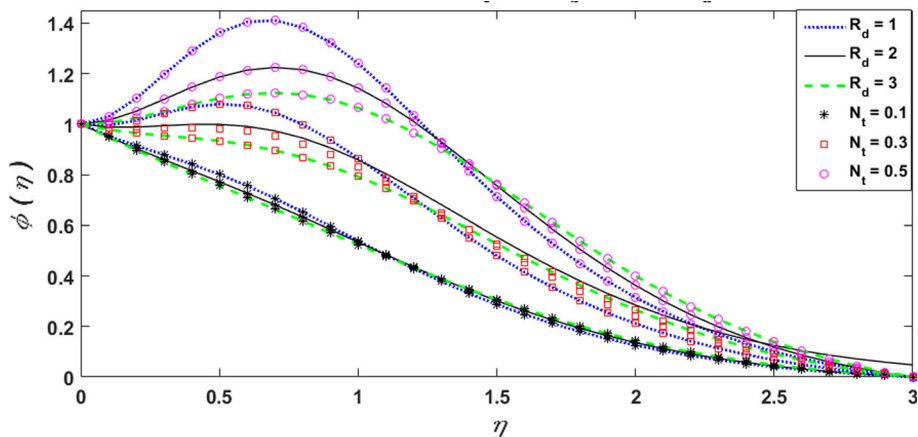**Fig. 3** Absolute error of N_t and R_d on $\theta(\eta)$

Fig. 4 Variation of N_t and R_d on $\phi(\eta)$

numbers graphically and numerically. The effect of error analysis is also described graphically for above-mentioned parameters. Numerical illustration of the results for local Nusselt number and local Sherwood number against different physical quantities is also provided, respectively, in Tables 1 and 2.

Figure 2 describes the effect of N_t along with R_d on θ profile, and results show that θ increases with increment in both N_t and R_d. The θ profile has highest value at $N_t = 0.5$ with $R_d = 3$ and then decreases with decrease in value of R_d. Also R_d values increase with increment in N_t. The larger values of thermophoretic parameter N_t depict large difference in tem-

perature θ and shear gradient. It is also observed from Fig. 1 that as the thermophoretic effect strengthens, then decreasing behavior is observed in the temperature gradient at the sheet. Thus increment in N_t will result large temperature inside boundary layer. Figure 3 describes error analysis between Adam's and BDF numerical methods. It is quite clear from figure that error in temperature profile $\phi(\eta)$ for various values of R_d and N_t is quite negligible and it exists in the range of 10^{-07}–10^{-10}. Figure 4 depicts the influence of N_t along with R_d on nanoparticle concentration profile. It can be observed from Fig. 4 that nanoparticle concentration profile increases with an increment in N_t but decreases with R_d. Figure 6

Fig. 5 Absolute error of N_t and R_d on $\phi(\eta)$
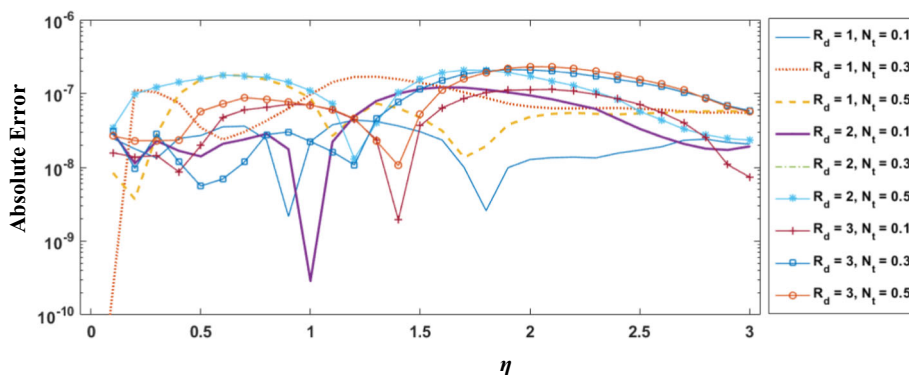
Fig. 6 Variation of N_t and R_d on local Nusselt number
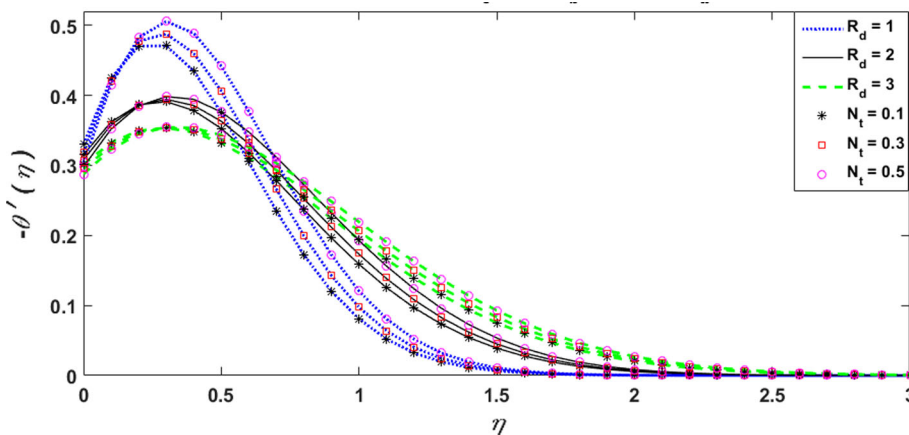
Fig. 7 Absolute error of N_t and R_d with local Nusselt number
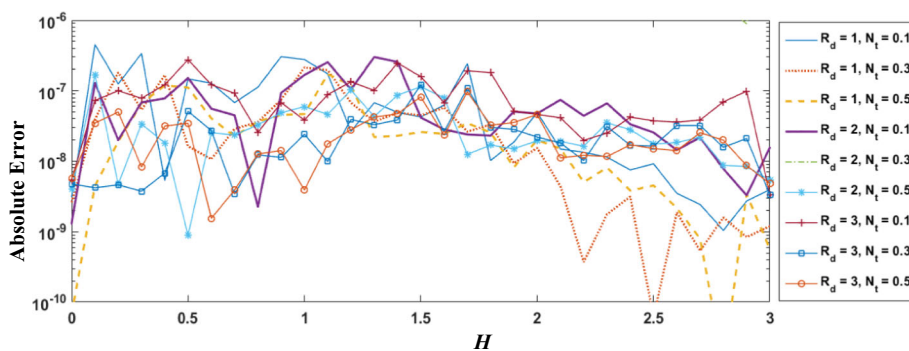
describes that local Nusselt number increases with increment in N_t but decreases with R_d, whereas decreasing trend is observed for local Sherwood number with an increment in N_t and R_d values as shown in Fig. 8. Figures 5 and 7 describe the error analysis by using two numerical approaches for nanoparticle concentration profile and local Nusselt number, respectively, and it exists in the range of 10^{-07} to 10^{-10} which is quite negligible, whereas the gauges of the error validate computational accuracy of the level around 10^{-7} (Figs. 6, 7).

The influence of N_b on θ profile along with R_d is shown in Fig. 8, which elucidates that θ profile increase with the increment in N_b while decreases with the increment in R_d. In nanofluids, the Brownian motion takes place because of

nanoparticles size having nanometer scale, and as a result, the effect of particles motion on nanofluid has a vital role in transfer of heat. According to Brownian motion definition, as values of N_b are increased, the nanoparticles kinetic energy also increases due to chaotic motion intensity, and as a result, temperature of nanofluid also increases. Figure 10 depicts that as the values of N_b are increased along with an increment in R_d, the values of nanoparticle concentration profile decreases. The local Nusselt number values increase with an increment in N_b and decrease in R_d values as shown in Fig. 10. Figures 9 and 11 elucidate the analysis of error with radiation parameter and local Nusselt number for Brownian motion parameter (N_b), respectively. It is quite clear from error analysis graphs that error lies in the range

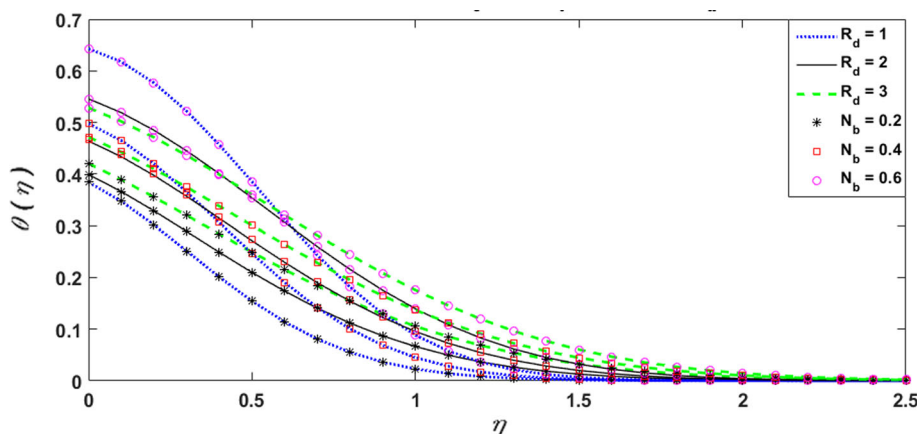**Fig. 8** Influence of N_b and R_d on $\theta(\eta)$

Fig. 9 Absolute error of N_b and R_d on $\theta(\eta)$
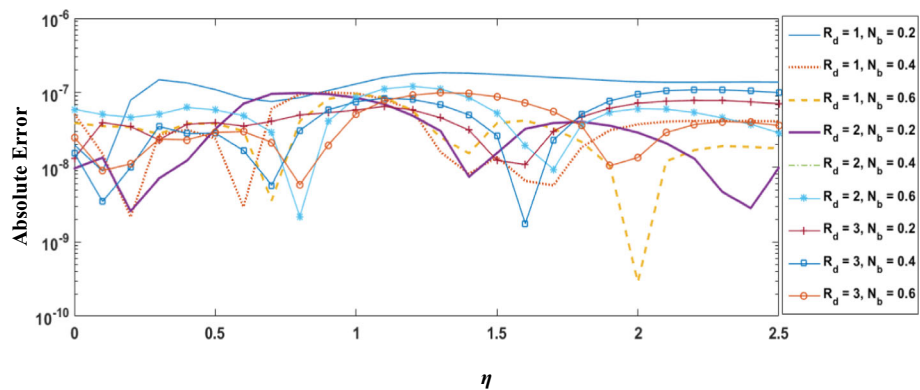

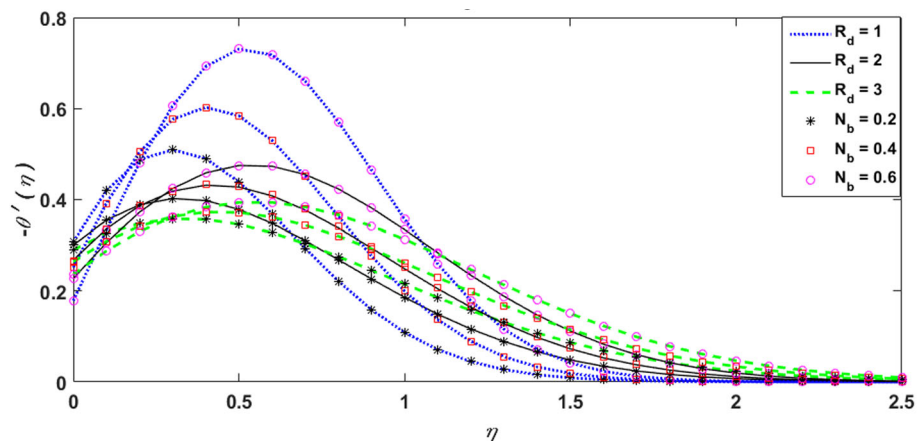**Fig. 10** Variation of N_b and R_d on local Nusselt number

Fig. 11 Absolute error of N_b and R_d on local Nusselt number
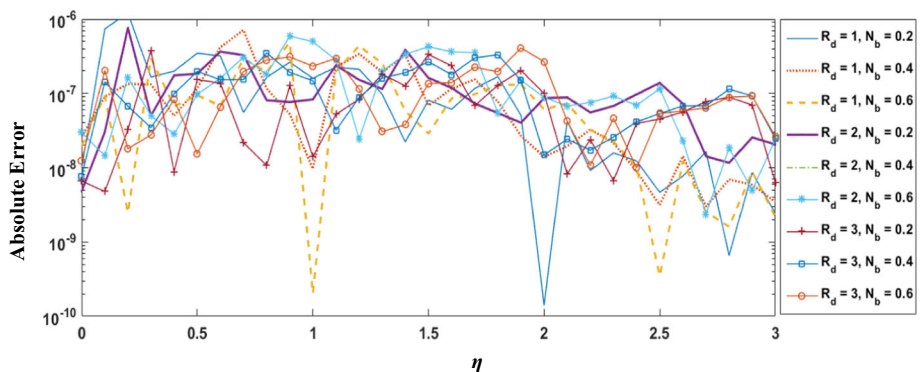
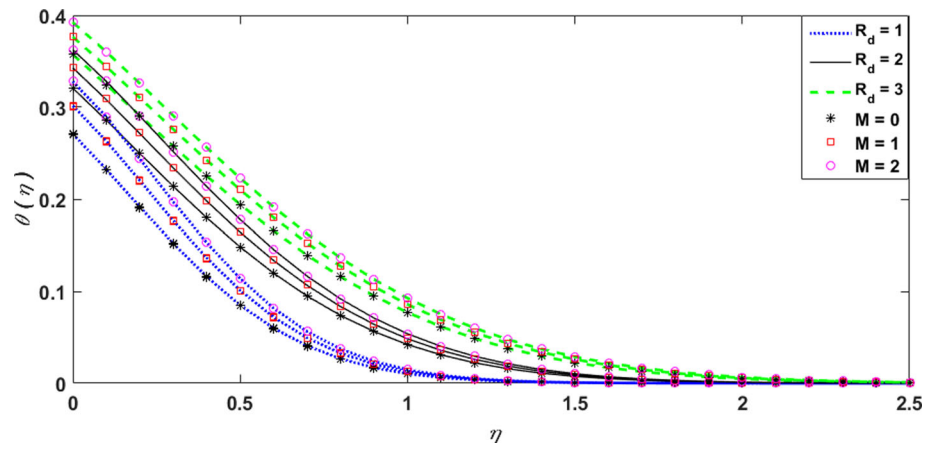**Fig. 12** Influence of M and R_d on $\theta(\eta)$

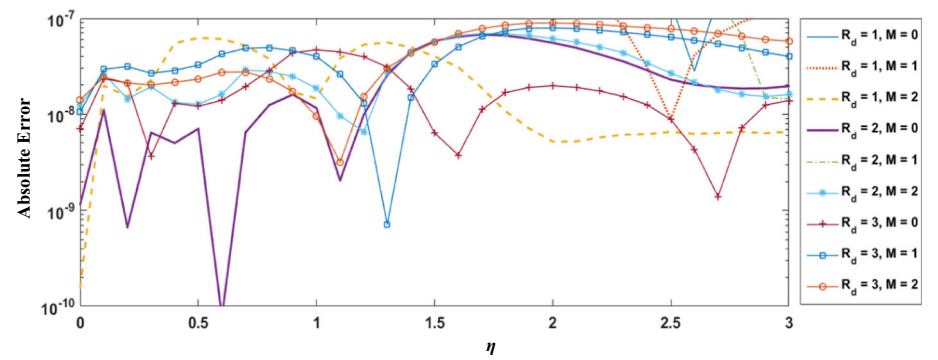**Fig. 13** Absolute error of M and R_d on $\theta(\eta)$

Fig. 14 Variation of M and R_d on local Nusselt number
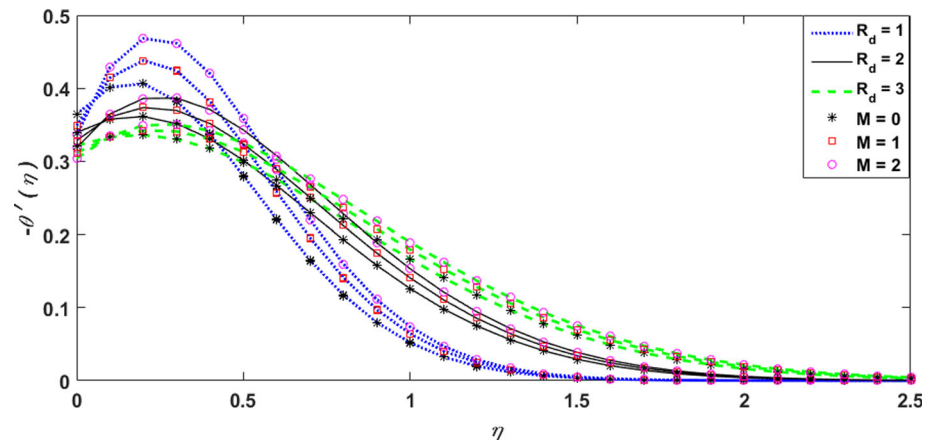
Fig. 15 Absolute error of M and R_d on local Nusselt number
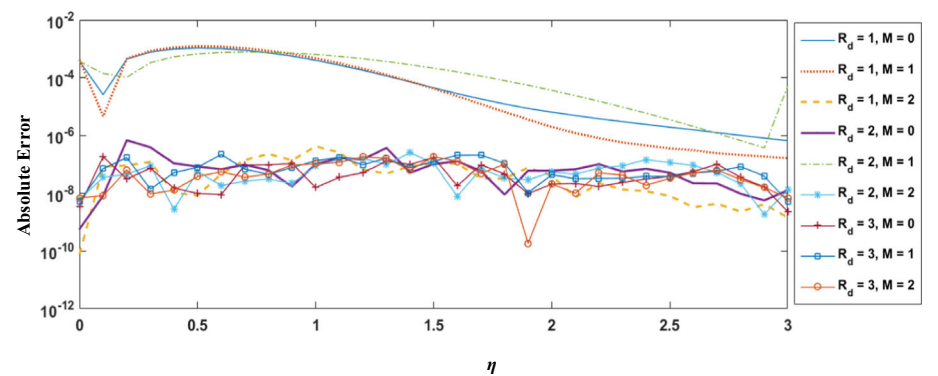
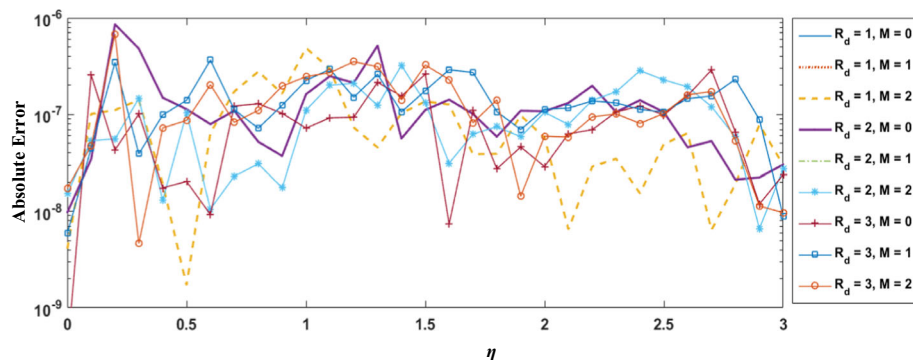**Fig. 16** Influence of M and R_d on local Sherwood number
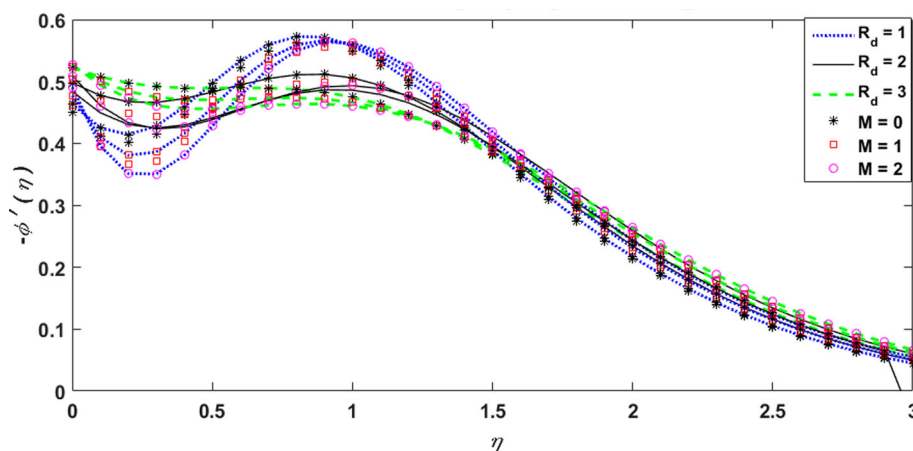
Fig. 17 Absolute error of M and R_d on local Sherwood number

of 10^{-06}–10^{-10} which is quite negligible and proves the validity (Figs. 10, 11).

The effect of M along with R_d on temperature profiles can be easily noticed in Fig. 12. It is quite clear from Fig. 12 that increasing trend is found for θ profile with an increment in M and R_d. One may also depict from Fig. 12 that the layer of thermal boundary increases as the strength of M is increased. The variation of M and R_d with local Nusselt number and local Sherwood number is depicted in Figs. 14 and 16. Figures 13, 15, 17 describe the error analysis of radiation parameter with temperature profile, local Nusselt number and local Sherwood number for M, respectively. It is observed from error analysis graphs that error lies in the range of 10^{-06}–10^{-10} which is quite negligible and proves the validity obtained results (Figs. 14, 15, 16, 17).

The variation in Le on $\theta(\eta)$ and radiation parameter is shown in Fig. 18. It is observed from Fig. 18 that increasing behavior is found for $\theta(\eta)$ with an increment in Le and R_d, whereas the influence of Le on concentration profile $\phi(\eta)$ and R_d is shown in Fig. 20. Figures 18 and 20 describe that with the gradually increase in Le will result in larger difference in temperature and a thinner concentration boundary layer due to weaker molecular diffusivity. The effect of local Nusselt number on Le and R_d is depicted in Figs. 22, and it is noticed that local Nusselt number initially increases with increment in Le and R_d, but later it decreases with an increase in Le

and R_d. While from Figs. 19, 21, 23, it is quite clear that error lies in the range of 10^{-06} to 10^{-10} for both temperature and concentration profiles as well as local Nusselt numbers (Figs. 20, 21, 22, 23) .

The effect of temperature profile $\theta(\eta)$ on Pr and R_d is presented in Fig. 24, and it is found from that $\theta(\eta)$ increases with decrease in Pr values and increases with an increment in R_d and depicts that an increment in Pr will result in decrease in thermal diffusivity, and as a result, the fluid temperature and thickness of thermal boundary layer decrease. The effect of local Nusselt number on Pr and R_d is shown in Fig. 26. Figures 25 and 27 describe the error analysis with Pr and R_d, for both temperature and Nusselt numbers. It is observed from error analysis graphs that error lies in the range of 10^{-07} to 10^{-10} which is quite negligible (Figs. 26, 27).

The effect of θ on E_c and R_d is presented in Fig. 28, and results show that increasing trend is observed in temperature profile $\theta(\eta)$ with increase in E_c and decrease in R_d, while E_c has inverse influence on θ as compared to Pr. From Fig. 30, it is noticed that local Nusselt number increases with increment in E_c, but with R_d, initially it increases but later it decreases with an increase in R_d. Figures 29 and 31 describe the error analysis graphs of E_c for temperature profiles as well as Nusselt numbers. It is noted that quite negligible error lies in the range of 10^{-07} to 10^{-10} (Figs. 30, 31).

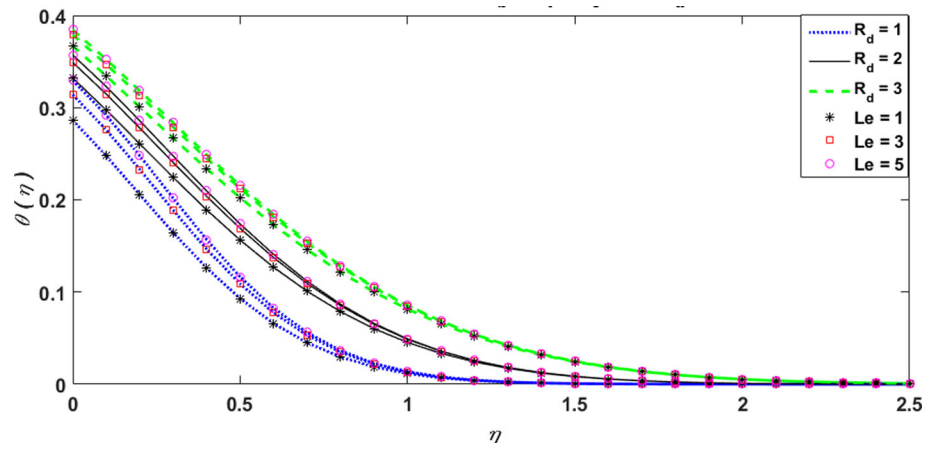**Fig. 18** Influence of Le and R_d on $\theta(\eta)$

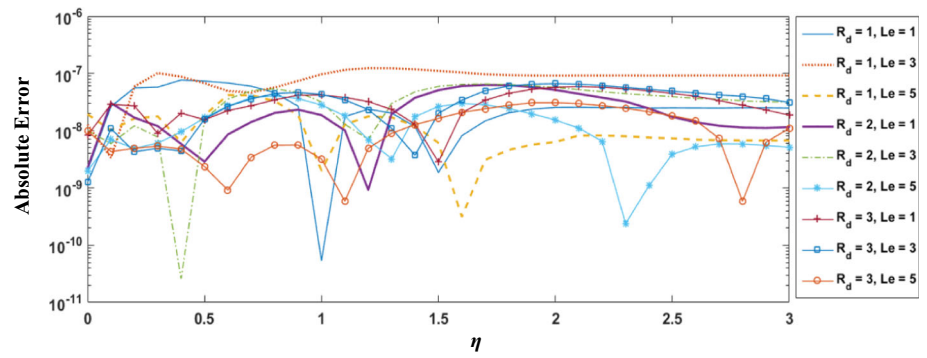**Fig. 19** Absolute error of Le and R_d on $\theta(\eta)$

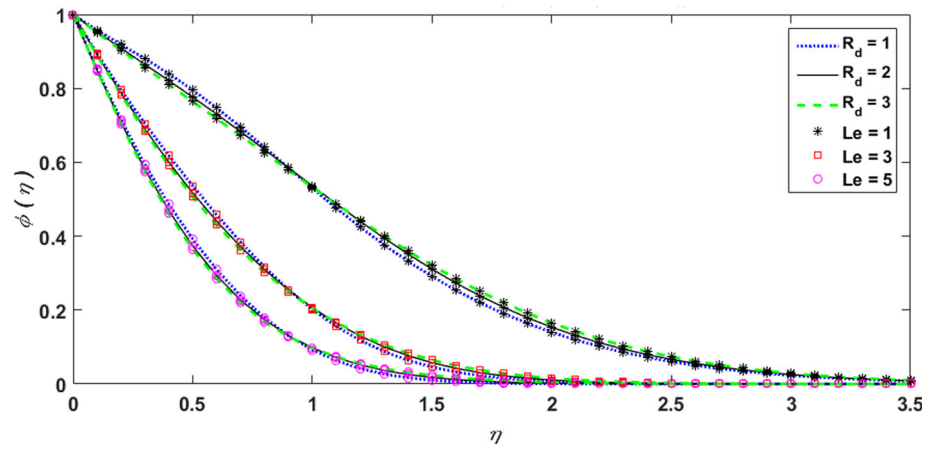**Fig. 20** Effect of Le and R_d on $\phi(\eta)$

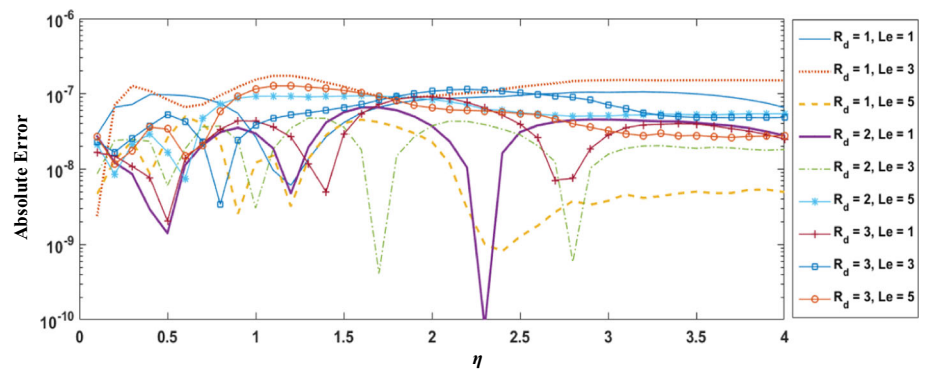**Fig. 21** Absolute error of Le and R_d on $\phi(\eta)$

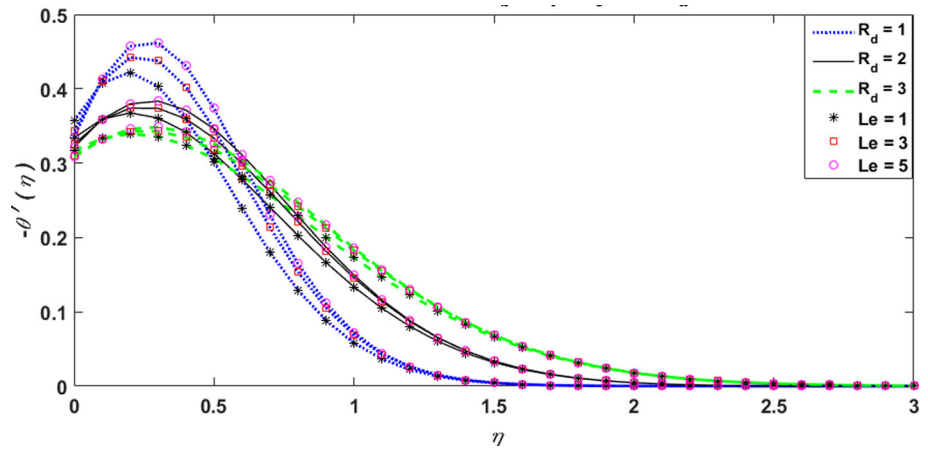**Fig. 22** Effect of Le and R_d on local Nusselt number

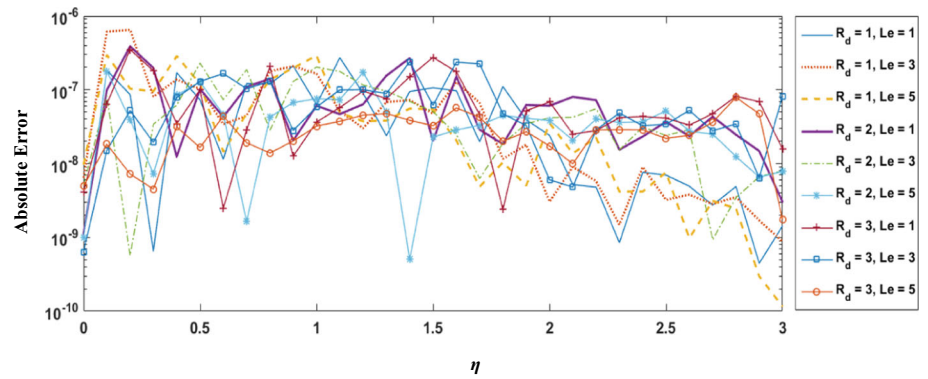**Fig. 23** Absolute error of Le and R_d on local Nusselt number

Fig. 24 Effect of Pr and R_d on $\theta(\eta)$
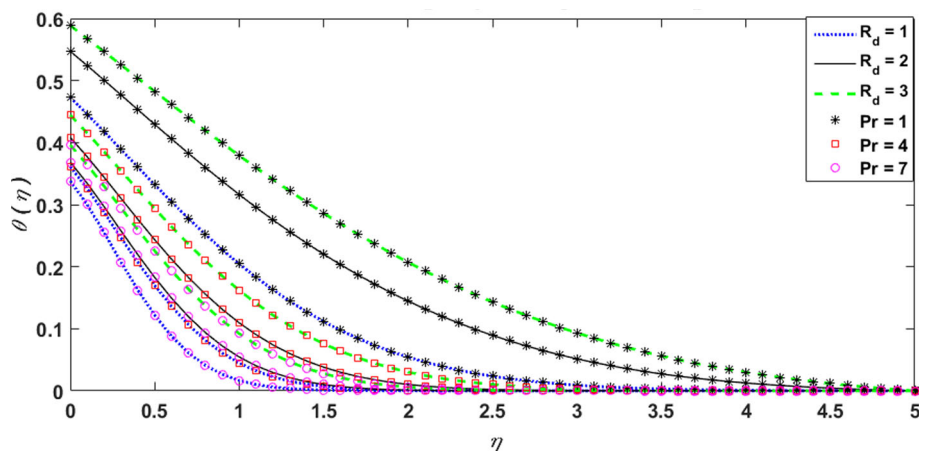

Fig. 25 Absolute error of Pr and R_d on $\theta(\eta)$
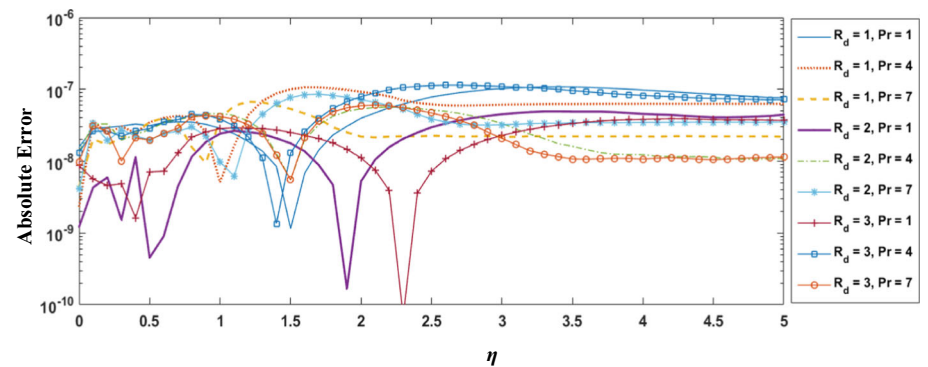
Fig. 26 Influence of Pr and R_d on local Nusselt number
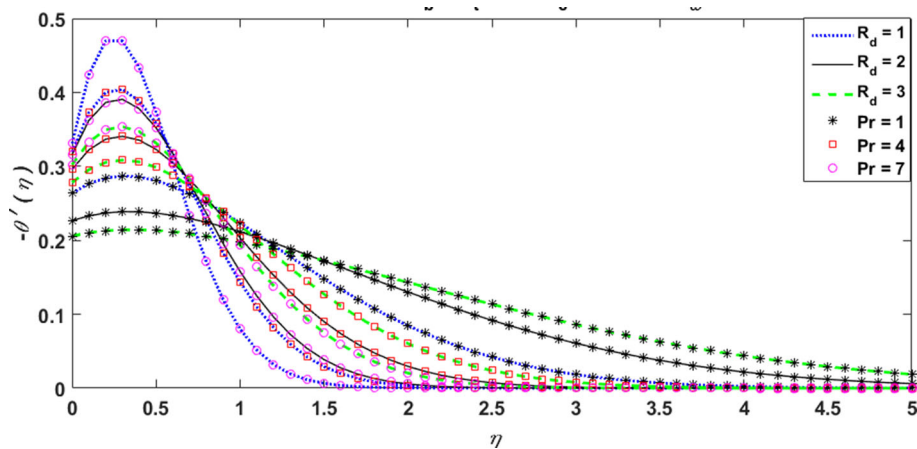
Fig. 27 Absolute error of Pr and R_d on local Nusselt number
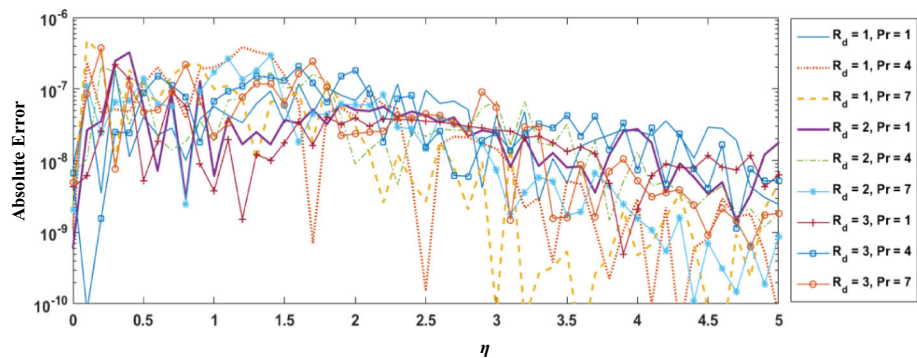
Fig. 28 Influence of E_c and R_d on $\theta(\eta)$
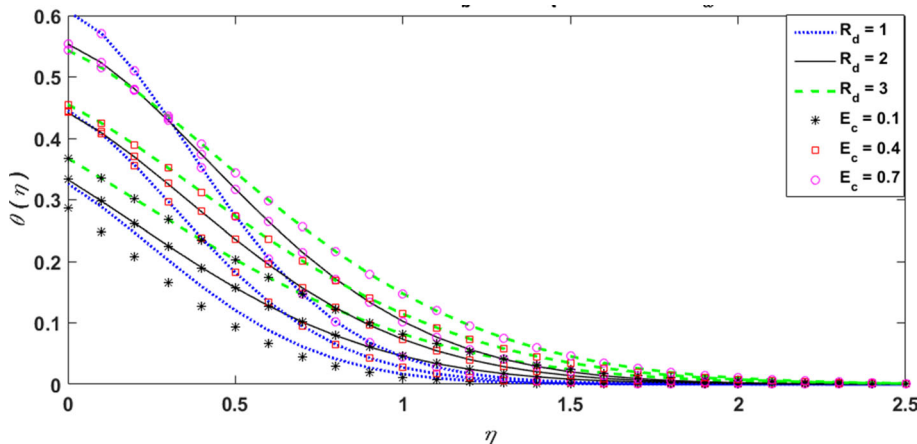
Fig. 29 Absolute error of E_c and R_d on $\theta(\eta)$
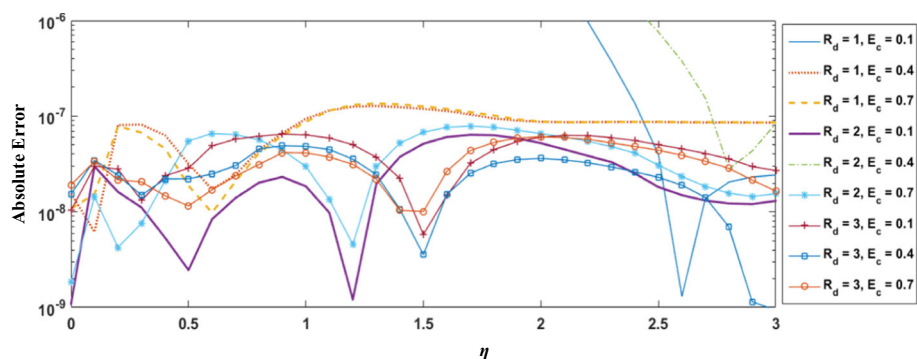
Fig. 30 Influence of E_c and R_d on local Nusselt number
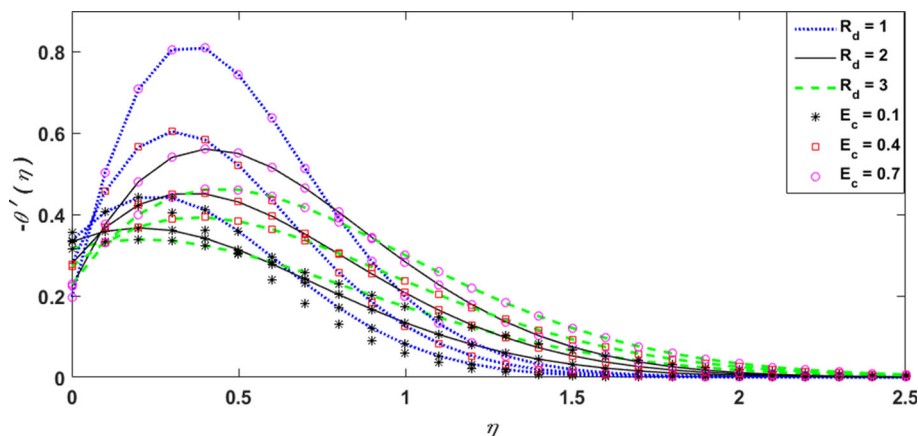
Fig. 31 Absolute error of E_c and R_d on local Nusselt number
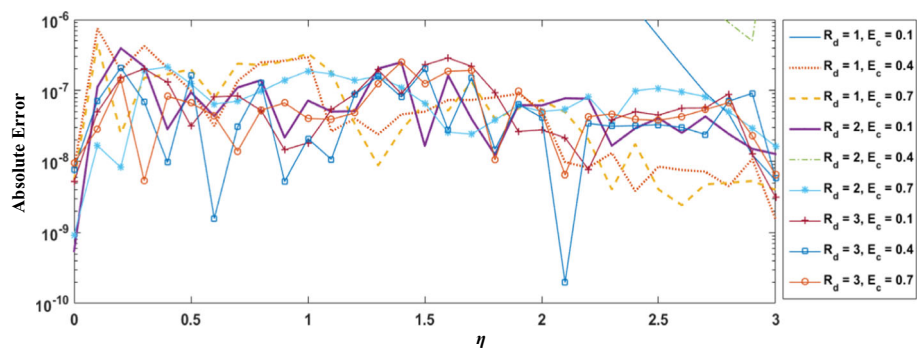
Fig. 32 Effect of γ and R_d on $\theta(\eta)$
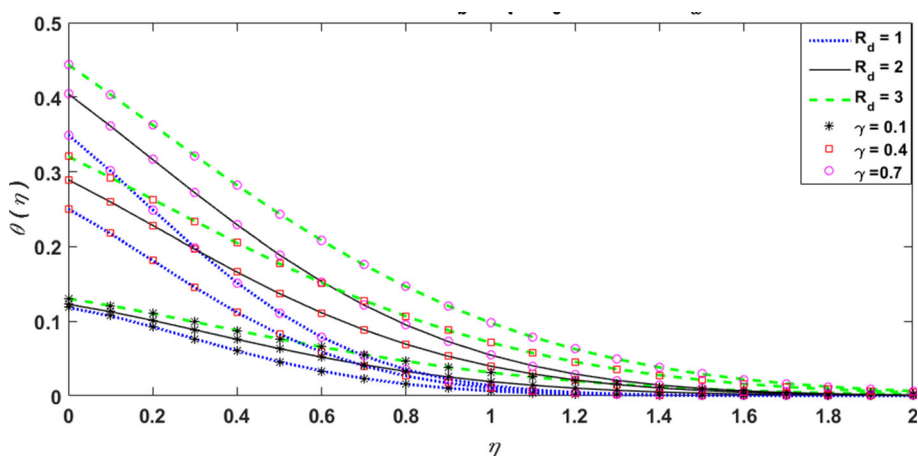
Fig. 33 Absolute error of γ and R_d on $\theta(\eta)$
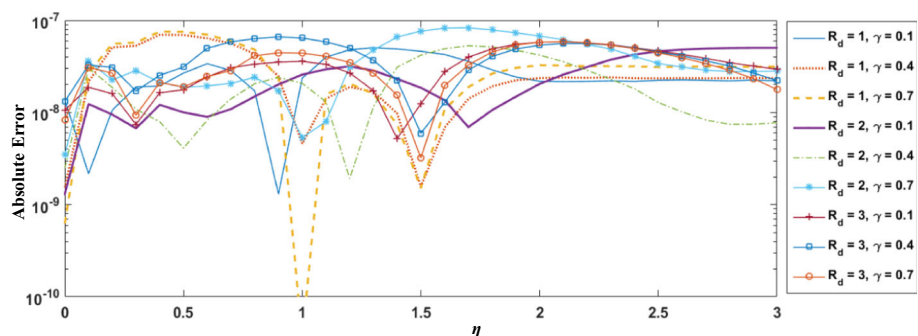
Fig. 34 Influence of γ and R_d on $\phi(\eta)$
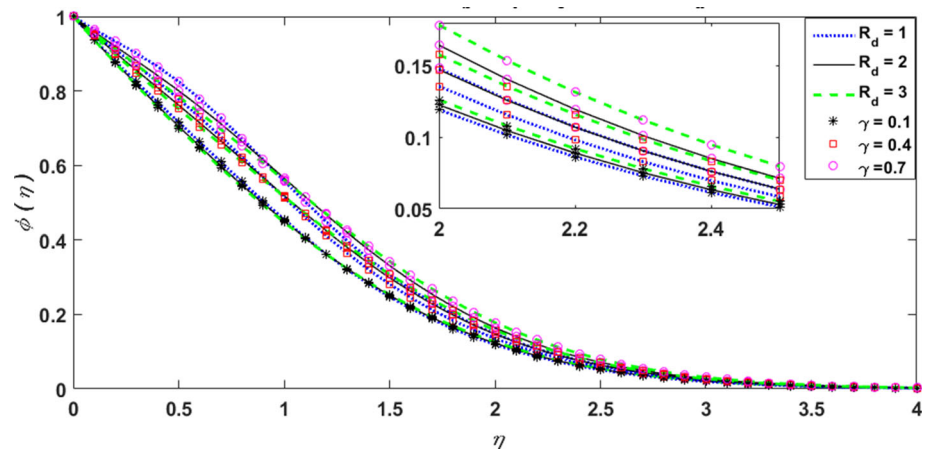
Fig. 35 Absolute error of γ and R_d on $\phi(\eta)$

Fig. 36 Influence of γ and R_d on local Nusselt number

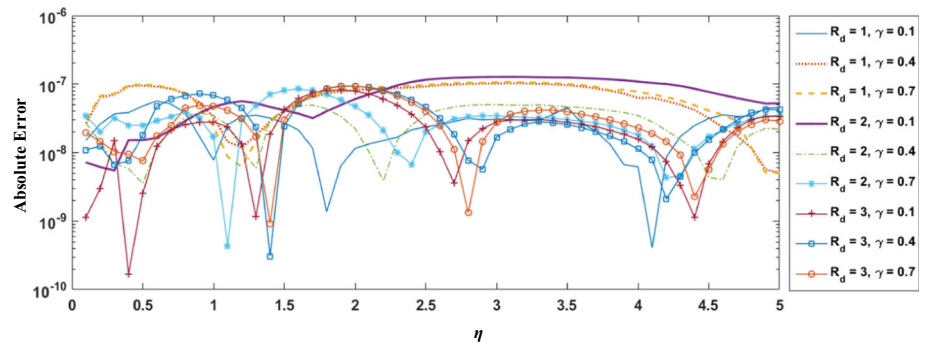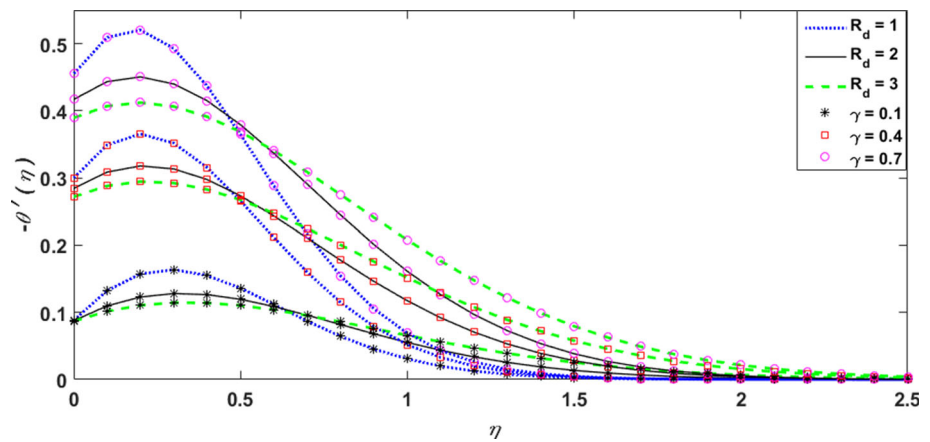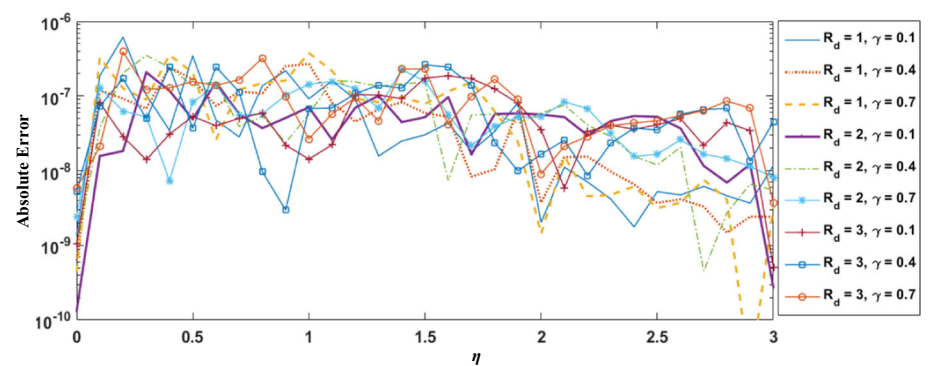**Fig. 37** Absolute error of γ and R_d on local Nusselt number

Table 3 Numerical values for skin friction coefficient with parameters $N_t = N_b = 0.1$, $\gamma = 0.5$, $Pr = Le = 1$ and $E_c = 0.1$

M	λ	$C_f (Re)^{1/2}$
0.5	0.5	0.8339562482545
1.0	0.5	0.8961318731107
1.5	0.5	0.955634960726
2.0	0.5	1.012717709835
1.0	0.1	1.482955821193
1.0	0.3	1.204441113306
1.0	0.5	0.8961318731107
1.0	0.7	0.5587871972135

The effect of Biot number γ on $\theta(\eta)$ and concentration $\phi(\eta)$ with radiation parameter is shown in Figs. 32 and 34, and it is found that value of both $\theta(\eta)$ and $\phi(\eta)$ increases with increment in both γ and R_d. The influence of local Nusselt number for γ and R_d is shown in Fig. 36. From Fig. 36, it is observed that the values of local Nusselt number increase with increment in γ and decrease in R_d. Error analysis graph for γ for both temperature and concentration profiles, as well as, Nusselt numbers, is shown in Figs. (33, 35 and 37). From these figures, it is quite clear that error lies in the range of 10^{-07}–10^{-10} which is quite negligible and shows the validity of computation (Figs. 34, 35, 36, 37).

Numerical illustrations for the results are presented in Tables 1 and 2 by variation of local Nusselt and Sherwood numbers for different physical quantities. The tabulated results established the convergence of the solutions on the basis of both Sherwood and Nusselt numbers. Additionally, the numerical values for skin friction coefficient with different parameters, i.e., M and λ, are listed in Table 3.

6 Convergence and Complexity Analysis

In this section, stability analysis is presented on the basis of different levels of accuracy goal for numerical computing algorithms. Additionally, the comparison of the complexity indices for Adams method (AM), backward difference method (BDF), explicit Runge–Kutta (ERK), implicit Runge–Kutta method (IRK) and extrapolation technique (ET) is presented.

Result of stability analysis and complexity operators on the basis of stiff and nonstiff accuracy goals, i.e., 10^{-05}, 10^{-10}, 10^{-15} and 10^{-20}, is calculated for AM, BDF, ERK, IRK and ET and are provided in Tables 4, 5, 6 and 7 for variation of Ec, M, Pr and Rd of fluidic model, respectively.

It can be seen that all five numerical methods are applicable for both nonstiff, i.e., 10^{-05} and 10^{-10}, and stiff, i.e., 10^{-15} and 10^{-20}, accuracy goals for all four variation of the fluidic model, which established the stability and convergence of the numerical procedures, whereas comparison

Table 4 Convergence and complexity measures of the system in case of $E_c = 0.1$

Method	Accuracy goal	Timing	Steps	Evaluation
Adams	10^{-20}	0.296875	107	186
	10^{-15}	0.328125	90	171
	10^{-10}	0.109375	85	181
	10^{-05}	0.046875	33	69
BDF	10^{-20}	3.20313	185	222
	10^{-15}	1.6875	169	207
	10^{-10}	0.5625	139	168
	10^{-05}	0.1875	41	48
ERK	10^{-20}	0.46875	55	883
	10^{-15}	0.328125	36	579
	10^{-10}	0.15625	16	259
	10^{-05}	0.078125	11	113
IRK	10^{-20}	3.25	61	832
	10^{-15}	2.875	54	812
	10^{-10}	2.25	42	665
	10^{-05}	0.78125	20	279
ET	10^{-20}	0.59375	79	925
	10^{-15}	0.515625	58	678
	10^{-10}	0.34375	35	476
	10^{-05}	0.1875	11	167

Table 5 Convergence and complexity measures of the system in case of $M = 1.0$

Method	Accuracy goal	Timing	Steps	Evaluation
Adams	10^{-20}	0.28125	108	193
	10^{-15}	0.2125	92	179
	10^{-10}	0.15625	90	169
	10^{-05}	0.0625	35	71
BDF	10^{-20}	4.32813	191	224
	10^{-15}	3.01563	176	216
	10^{-10}	0.59375	145	172
	10^{-05}	0.1875	42	50
ERK	10^{-20}	0.390625	57	915
	10^{-15}	0.34375	37	596
	10^{-10}	0.19625	17	275
	10^{-05}	0.165625	12	123
IRK	10^{-20}	1.09375	61	824
	10^{-15}	1.17188	52	764
	10^{-10}	1.13438	43	681
	10^{-05}	0.578125	20	273
ET	10^{-20}	1.03125	40	854
	10^{-15}	0.5625	24	614
	10^{-10}	0.453125	13	421
	10^{-05}	0.171875	11	167

Table 6 Convergence and complexity indices for the model in case of $Pr = 4$

Method	Accuracy Goal	Timing	Steps	Evaluation
Adams	10^{-20}	0.359375	90	155
	10^{-15}	0.26875	74	139
	10^{-10}	0.09375	70	111
	10^{-05}	0.03125	28	57
BDF	10^{-20}	3.26563	145	174
	10^{-15}	2.28125	130	159
	10^{-10}	0.484375	112	134
	10^{-05}	0.171875	35	41
ERK	10^{-20}	0.359375	51	819
	10^{-15}	0.28125	31	499
	10^{-10}	0.140625	13	211
	10^{-05}	0.0625	11	113
IRK	10^{-20}	2.9375	53	696
	10^{-15}	0.703125	46	662
	10^{-10}	0.640625	36	563
	10^{-05}	0.258125	17	235
ET	10^{-20}	0.421875	40	750
	10^{-15}	0.25	24	512
	10^{-10}	0.28125	13	335
	10^{-05}	0.0625	11	167

Table 7 Convergence and complexity measure of the system in case of $R_d = 2$

Method	Accuracy Goal	Timing	Steps	Evaluation
Adams	10^{-20}	0.378125	80	138
	10^{-15}	0.3375	70	135
	10^{-10}	0.109375	67	115
	10^{-05}	0.06875	27	55
BDF	10^{-20}	3.89063	135	158
	10^{-15}	3.29688	120	143
	10^{-10}	0.53125	104	126
	10^{-05}	0.140625.	33	39
ERK	10^{-20}	0.59375	50	803
	10^{-15}	0.265625	30	483
	10^{-10}	0.109375	12	195
	10^{-05}	0.0625	11	113
IRK	10^{-20}	1.125	52	687
	10^{-15}	0.59375	43	627
	10^{-10}	0.5	34	537
	10^{-05}	0.453125	17	221
ET	10^{-20}	0.34375	40	730
	10^{-15}	0.21875	24	482
	10^{-10}	0.203125	13	325
	10^{-05}	0.09375	11	167

of the complexity indices based on time, step and function evaluations shows that for better accuracy goals, the complexity of the all five numerical computing algorithm increases. However, it is found that on average the Adams numerical procedure is the most efficient from the rest of computing methodologies.

7 Conclusions and Future Recommendations

In this work, strength of numerical solvers has been exploited to analyze the dynamics of the system model based on laminar two-dimensional nanofluid flow over stretching sheet. We have investigated the effect of radiation parameter along with thermophoresis parameter, Brownian motion parameter, magnetic field parameter, Lewis Number, Prandtl Number, Eckert number, Biot number on temperature profile $\theta(\eta)$, nanoparticle concentration profile $\phi(\eta)$, local Nusselt and local Sherwood number through sufficient number of graphically and numerical illustration. Following are the main outcomes.

- Temperature profile $\theta(\eta)$ increases with increment in thermophoresis parameter, Brownian motion parameter, magnetic field parameter, Lewis number, Eckert number and Biot number while temperature profile $\theta(\eta)$ decreases with the increment in Prandtl number.
- Increasing trend is observed for nanoparticle concentration profile $\phi(\eta)$ with an increment in thermophoresis parameter, magnetic field parameter, Lewis Number, Prandtl Number and Biot number while concentration profile decreases with an increment in Brownian motion parameter.
- Local Nusselt number enhances with an increment in thermophoresis parameter, Brownian motion parameter, magnetic field parameter, Lewis number, Eckert number and Biot number
- Local Sherwood number increases with an increment in Brownian motion parameter and Lewis number, while its value decreases with an increment in thermophoresis parameter, magnetic field parameter, Eckert number and Biot number.
- Error analysis lies in the range of 10^{-07}–10^{-10} which is quite negligible and shows the validity of computation.

In future, one may explore/exploit the strength of intelligent computing paradigm for solving fluid dynamics problems arising in diversified field of applied science and technology [35–40].

Compliance with Ethical Standards

Conflict of interest The authors declare that they have no known competing financial interests or personal relationships that could have appeared to influence the work reported in this paper.

References

1. Kim, S.; Mor, G.K.; Paulose, M.; Varghese, O.K.; Shankar, K.; Grimes, C.A.: Broad spectrum light harvesting in TiO $ _2 $ nanotube array-hemicyanine dye–P3HT hybrid solid-state solar cells. IEEE J. Sel. Top. Quantum Electron. **16**(6), 1573–1580 (2010)

2. De Wild, J.; Duindam, T.F.; Rath, J.K.; Meijerink, A.; Van Sark, W.G.J.H.M.; Schropp, R.E.I.: Increased up conversion response in a-Si: H solar cells with broad-band light. IEEE J. Photovolt. **3**(1), 17–21 (2013)

3. Hua, X.; Zeng, Y.; Wang, W.; Shen, W.: Light absorption mechanism of c-Si/a-Si Half-coaxial nanowire arrays for nanostructured hetero junction photovoltaics. IEEE Trans. Electron Devices **61**(12), 4007–4013 (2014)

4. Pakhuruddin, M.Z.; Huang, J.; Dore, J.; Varlamov, S.: Light absorption enhancement in laser-crystallized silicon thin films on textured glass. IEEE J. Photovolt. **6**(1), 159–165 (2016)

5. Ishizaki, K.; Motohira, A.; De Zoysa, M.; Tanaka, Y.; Umeda, T.; Noda, S.: Microcrystalline-silicon solar cells with photonic crystals on the top surface. IEEE J. Photovolt. **7**(4), 950–956 (2017)

6. Chen, M.; Zhang, Y.; Cui, Y.; Zhang, F.; Qin, W.; Zhu, F.; Hao, Y.: Profiling light absorption enhancement in two-dimensional photonic-structured perovskite solar cells. IEEE J. Photovolt. **7**(5), 1324–1328 (2017)

7. Mehmood, U.; Al-Ahmed, A.; Afzaal, M.; Hakeem, A.S.; Haladu, S.A.; Al-Sulaiman, F.A.: Enhancement of the photovoltaic performance of a dye-sensitized solar cell by cosensitizing TiO2 photoanode with spray-coated uncapped PbS nanocrystals and ruthenizer. IEEE J. Photovolt. **8**(2), 512–516 (2018)

8. Liang, H.; Liu, Y.; Li, H.; Zhang, H.; Han, S.; Wu, Y.; Wang, Z.: All-fiber light intensity detector based on an ionic-liquid-adorned microstructured optical fiber. IEEE Photonics J. **10**(2), 1–8 (2018)

9. Ishii, S.; Sugavaneshwar, R.P.; Nagao, T.: Titanium nitride nanoparticles as plasmonic solar heat transducers. J. Phys. Chem. C **120**(4), 2343–2348 (2016)

10. Raffaelle, R.P.; Landi, B.J.; Evans, C.M.; Cress, C.D.; Andersen, J.; Castro, S.L.; Bailey, S.G.: Nanomaterial development for polymeric solar cells. In: 2006 IEEE 4th world conference on photovoltaic energy conference, (vol. 1, pp. 186–189). IEEE, 2006

11. Gondal, M.A.; Rashid, S.G.; Dastageer, M.A.; Zubair, S.M.; Ali, M.A.; Lienhard, J.H.; McKinley, G.H.; Varanasi, K.K.: Sol-Gel synthesis of Au/Cu-TiO2 nanocomposite and their morphological and optical properties. IEEE Photonics J. **5**(3), 2201908–2201908 (2013)

12. Hogan, N.J.; Urban, A.S.; Ayala-Orozco, C.; Pimpinelli, A.; Nordlander, P.; Halas, N.J.: Nanoparticles heat through light localization. Nano Lett. **14**(8), 4640–4645 (2014)

13. Ishii, S.; Sugavaneshwar, R.P.; Chen, K.; Dao, T.D.; Nagao, T.: Solar water heating and vaporization with silicon nanoparticles at mie resonances. Opt. Mater. Express **6**(2), 640–648 (2016)

14. Hameed, A.H.; Salih, S.R.; Balage, S. :Direct absorption solar collector with direct heat exchange in inclined receiver unit.

15. Wang, Z.; Tao, P.; Liu, Y.; Xu, H.; Ye, Q.; Hu, H.; Song, C.; Chen, Z.; Shang, W.; Deng, T.: Rapid charging of thermal energy storage materials through plasmonic heating. Sci. Rep **4**, 6246 (2014)

16. Mushtaq, A.; Mustafa, M.; Hayat, T.; Alsaedi, A.: Nonlinear radiative heat transfer in the flow of nanofluid due to solar energy: a

17. numerical study. J. Taiwan Inst. Chem. Eng. **45**(4), 1176–1183 (2014)

17. Ghasemi, S.E.; Hatami, M.; Jing, D.; Ganji, D.D.: Nanoparticles effects on MHD fluid flow over a stretching sheet with solar radiation: a numerical study. J. Mol. Liq. **219**, 890–896 (2016)

18. Awan, S.E.; et al.: Dynamical analysis for nanofluid slip rheology with thermal radiation, heat generation/absorption and convective wall properties. AIP Adv. **8**(7), 075122 (2018)

19. Awan, S.E.; et al.: Numerical treatment for hydro-magnetic unsteady channel flow of nanofluid with heat transfer. Res. Phys. **9**, 1543–1554 (2018)

20. Mahanthesh, B.; Gireesha, B.J.; Gorla, R.R.; Abbasi, F.M.; Shehzad, S.A.: Numerical solutions for magnetohydrodynamic flow of nanofluid over a bidirectional non-linear stretching surface with prescribed surface heat flux boundary. J. Magn. Magn. Mater. **417**, 189–196 (2016)

21. Mahanthesh, B.; Shashikumar, N.S.; Gireesha, B.J.; Animasaun, I.L.: Effectiveness of Hall current and exponential heat source on unsteady heat transport of dusty TiO2-EO nanoliquid with nonlinear radiative heat. J. Comput. Des. Eng. **6**(4), 551–561 (2019)

22. Awais, M.; et al.: Hydromagnetic mixed convective flow over a wall with variable thickness and Cattaneo–Christov heat flux model: OHAM analysis. Res. Phys. **8**, 621–627 (2018)

23. Mahanthesh, B.; Gireesha, B.J.; Manjunatha, S.; Gorla, R.S.R.: Effect of viscous dissipation and Joule heating on three-dimensional mixed convection flow of nano fluid over a non-linear stretching sheet in presence of solar radiation. J. Nanofluids **6**(4), 735–742 (2017)

24. Mahanthesh, B.; Gireesha, B.J.; Animasaun, I.L.; Muhammad, T.; Shashikumar, N.S.: MHD flow of SWCNT and MWCNT nanoliquids past a rotating stretchable disk with thermal and exponential space dependent heat source. Phys. Scr. **94**(8), 085214 (2019)

25. Lin, Y.; Jiang, Y.: Effects of Brownian motion and thermophoresis on nanofluids in a rotating circular groove: a numerical simulation. Int. J. Heat Mass Transf. **123**, 569–582 (2018)

26. Lin, Y.; Li, B.; Zheng, L.; Chen, G.: Particle shape and radiation effects on Marangoni boundary layer flow and heat transfer of copper-water nanofluid driven by an exponential temperature. Powder Technol. **301**, 379–386 (2016)

27. Lin, Y.; Zheng, L.; Chen, G.: Unsteady flow and heat transfer of pseudo-plastic nanoliquid in a finite thin film on a stretching surface with variable thermal conductivity and viscous dissipation. Powder Technol. **274**, 324–332 (2015)

28. Lin, Y.; Zheng, L.; Zhang, X.; Ma, L.; Chen, G.: MHD pseudo-plastic nanofluid unsteady flow and heat transfer in a finite thin film over stretching surface with internal heat generation. Int. J. Heat Mass Transf. **84**, 903–911 (2015)

29. Shashikumar, N.S.; Gireesha, B.J.; Mahanthesh, B.; Prasannakumara, B.C.: Brinkman–Forchheimer flow of SWCNT and MWCNT magneto-nanoliquids in a microchannel with multiple slips and Joule heating aspects. Multidiscip. Model. Mater. Struct. (2018). https://doi.org/10.1108/MMMS-01-2018-0005

30. Mehmood, A.; et al.: Design of neuro-computing paradigms for nonlinear nanofluidic systems of MHD Jeffery-Hamel flow. J. Taiwan Inst. Chem. Eng. **91**, 57–85 (2018)

31. Amala, S.; Mahanthesh, B.: Hybrid nanofluid flow over a vertical rotating plate in the presence of hall current, nonlinear convection and heat absorption. J Nanofluids **7**(6), 1138–1148 (2018)

32. Mahanthesh, B.; Gireesha, B.J.; Gorla, R.S.; Makinde, O.D.: Magnetohydrodynamic three-dimensional flow of nanofluids with slip and thermal radiation over a nonlinear stretching sheet: a numerical study. Neural Comput. Appl. **30**(5), 1557–1567 (2018)

33. Krupalakshmi, K.L.; Gireesha, B.J.; Mahanthesh, B.; Gorla, R.S.R.: Influence of nonlinear thermal radiation and magnetic field on upperconvected Maxwell fluid flow due to a convectively heated

stretching sheet in the presence of dust particles. Commun. Numer. Anal (ISPACS) **2016**, 57–73 (2016)

34. Gireesha, B.J.; Gorla, R.S.R.; Mahanthesh, B.: Effect of suspended nanoparticles on three-dimensional MHD flow, heat and mass transfer of radiating Eyring–Powell fluid over a stretching sheet. J. Nanofluids **4**(4), 474–484 (2015)

35. Mehmood, A.; et al.: Intelligent computing to analyze the dynamics of Magnetohydrodynamic flow over stretchable rotating disk model. Appl. Soft Comput. **67**, 8–28 (2018)

36. Ahmad, I.; et al.: Intelligent computing to solve fifth-order boundary value problem arising in induction motor models. Neural Comput. Appl. **29**(7), 449–466 (2018)

37. Raja, M.A.Z.; Ahmed, T.; Shah, S.M.: Intelligent computing strategy to analyze the dynamics of convective heat transfer in MHD slip flow over stretching surface involving carbon nanotubes. J. Taiwan Inst. Chem. Eng. **80**, 935–953 (2017)

38. Umar, M.; et al.: Intelligent computing for numerical treatment of nonlinear prey–predator models. Appl. Soft Comput. **80**, 506–524 (2019)

39. Raja, M.A.Z.; Niazi, S.A.; Butt, S.A.: An intelligent computing technique to analyze the vibrational dynamics of rotating electrical machine. Neurocomputing **219**, 280–299 (2017)

40. Mehmood, A.; et al.: Integrated intelligent computing paradigm for the dynamics of micropolar fluid flow with heat transfer in a permeable walled channel. Appl. Soft Comput. **79**, 139–162 (2019)